ACS OMEGA

Open Access

http://pubs.acs.org/journal/acsodf

Article

Modification in Toxicity of L-Histidine-Incorporated ZnO Nanoparticles toward *Escherichia coli*

Shraddha Mahakal, Habib M. Pathan, Mohit Prasad, Sachin Rondiya, Shashikant P. Patole,* and Sandesh R. Jadkar*

Cite This: *ACS Omega* 2023, 8, 34354−34363

Read Online

ACCESS | Metrics & More | Article Recommendations | Supporting Information

ABSTRACT: This paper presents a comparative study of the toxicity of pristine-ZnO and L-histidine-incorporated ZnO toward *Escherichia coli* (*E. coli*) as a Gram-negative model organism. Pristine-ZnO and L-histidine-incorporated ZnO with different L-histidine concentrations were synthesized using an open aqueous solution bath technique. XRD studies revealed the formation of polycrystalline wurtzite ZnO. The average crystallite size of the synthesized L-histidine-incorporated ZnO decreased as the concentration of L-histidine increased. The FTIR spectra showed the presence of Zn−O, CO_2^-/CO_3^-, and C−N (only in L-histidine-incorporated ZnO samples) and −OH bond vibration signals in all samples. The chemical purity of all the samples was ensured using XPS analysis. The microbial activity of these samples was investigated using *E. coli*. The solution with 100 μg/mL ZnO in sterile distilled water showed up to 94% growth inhibition of *E. coli*, establishing antibacterial activity. However, L-histidine incorporated in ZnO showed reduced antibacterial activity with the increase of the concentration of L-histidine in ZnO. Furthermore, flow cytometry studies during the interaction of ZnO and *E. coli* confirmed the generation of reactive oxygen species (ROS), validating its antibacterial activity. The interaction of L-histidine-incorporated ZnO and *E. coli* showed declining ROS with the increase in the L-histidine concentration, indicating a ZnO toxicity reduction.

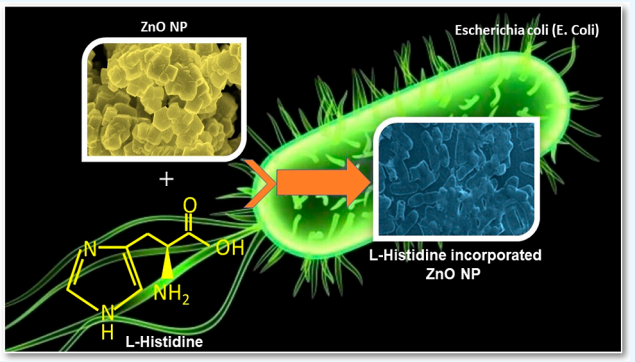

1. INTRODUCTION

Zinc oxide (ZnO) is a II−VI compound semiconductor with a direct, wide band gap of 3.34 eV at room temperature and an excitation binding energy of 60 meV, which is 2.4 times the thermal energy at room temperature.[1] Recently, ZnO and ZnO-based materials have been proven to be promising candidates for several functional applications such as semiconductor designing,[2] UV detectors,[3] antibacterial purposes,[4] biosensors,[5] drug delivery,[6] light-emitting diodes (LEDs), solar cells,[7] and so forth. ZnO has been studied extensively in bulk, thin films, or nanoparticles/nanostructures. It is a well-known fact that ZnO at the nanoscale dimension exhibits exceptional optical, electrical, magnetic, and chemical (viz. catalytic activity, etc.) properties when compared to its bulk counterpart of the same chemical composition.[8] Nanoscale ZnO has been realized in various forms/structures, such as nanorods, nanobelts, nanowires, nanocombs, nanoflowers, and so forth. It is mainly achieved by controlling the different physicochemical parameters, including the solvent system, precursor moieties, temperature, pH conditions during the synthesis of nanoparticles, and so forth.

Several methods like chemical vapor deposition (CVD),[9] metal−organic CVD (MOCVD),[10] pulsed laser deposition (PLD),[11] sol−gel,[12] hydrothermal, solvothermal,[13] precipitation,[14] and thermal decomposition methods[15] are routinely adopted to synthesize ZnO nanoparticles in the desired shape and size.[16] Based on the application, the appropriate methodology is adopted. Recently, the bioinspired synthesis of metal-oxide-based bioinorganic nanocomposites, especially nanosized ZnO, has drawn significant interest.[17,18] Integrating various amino acids,[19] surfactants,[20] or peptides[21] during nanoparticle synthesis leads to different physiobiological properties of the newly synthesized nanocomposites. *Glutamine*, *histidine*, and *glycine* were employed to study the variation in the morphology of ZnO synthesized by the hydrothermal method.[22] The integration of amino acids (due to their zwitterionic nature) leads to a strong surface association with the nanoparticles.[23] Gerstel et al.[24] have systematically studied the suitability of amino acids and dipeptides as structure-

Received: February 21, 2023
Accepted: June 2, 2023
Published: September 13, 2023

https://doi.org/10.1021/acsomega.3c01183
ACS Omega 2023, 8, 34354−34363

directing agents for the deposition of ZnO films. Brif et al.[25] have successfully demonstrated the incorporation of amino acids into ZnO and, consequentially, the engineering of its band gap due to the induced strain. Umetsu et al.[26] used artificial peptides to synthesize flower-like ZnO nanostructures at room temperature. In a review, Limo et al.[27] highlighted using biomolecules to control growth, modify the physicochemical properties, and their applications as biocomposites. ZnO exhibits excellent antibacterial activity against *E. coli*, *Pseudomonas*, *Staphylococcus aureus*, *Micrococcus*,[28] *P. mirabilis*, and *Salmonella typhi*.[29]

In the present work, we report the influence of L-histidine-incorporated ZnO on the antibacterial activity of a Gram-negative model organism, *E. coli*. For this, pristine-ZnO and L-histidine-incorporated ZnO were prepared for different concentrations of L-histidine. Furthermore, the structural and morphological properties of pristine-ZnO and L-histidine-incorporated ZnO were investigated using various techniques. Finally, the antibacterial activity of pristine-ZnO and L-histidine incorporated ZnO was analyzed using *E. coli*. We found that the antibacterial activity of L-histidine-incorporated ZnO critically depends on the concentration of L-histidine. It decreases with an increase in L-histidine concentration. The validation of antibacterial activity was confirmed by generating reactive oxygen species (ROS) using flow cytometry studies. Furthermore, the interaction of L-histidine-incorporated ZnO and *E. coli* shows decreasing ROS with increased L-histidine concentration, indicating a reduction in ZnO toxicity.

2. EXPERIMENTAL SECTION

2.1. Materials and Synthesis. The protocol used for synthesizing pristine-ZnO and L-histidine-incorporated ZnO powder using an open aqueous solution bath technique is provided in Supporting Information Figure S1. The ZnO sample prepared without L-histidine is labeled as pristine-ZnO. The concentration of L-histidine in ZnO was varied as 0.025, 0.05, 0.075, and 1.0 mg/mL, and the corresponding samples were labeled as ZnO-H1, ZnO-H2, ZnO-H3, and ZnO-H4, respectively.

2.2. Characterization. X-ray diffraction (XRD) (Bruker D8-ADVANCE) was used to study the structural properties of the synthesized samples. Ni-filtered Cu-K_α radiation at 1.542 Å was used for recording the XRD pattern in the $\theta-2\theta$ scanning mode. The recorded XRD data was subsequently subjected to Rietveld refinement for further analysis. The morphology of the synthesized particles was studied using field emission scanning electron microscopy (FESEM, Nova NanoSEM-450). The chemical environment of Zn and O in ZnO and Zn, O, and N in all the ZnO-H*i* (i = 1, 2, 3, 4) samples was probed by X-ray photoelectron spectroscopy (XPS). The spectra were recorded on beam line-14 installed on Indus-2 (2.5 GeV) synchrotron sources at the RRCAT, Indore, India. The base pressure of the working chamber was 3×10^{-8} mbar. The incident radiation with a photon energy of 4403 eV was used as the X-ray source. The photoelectrons ejected from the samples were analyzed by a concentric hemispherical analyzer (15 keV Phoibos 225) having a net resolution of 1 eV and a constant pass energy of 150 eV. The spectrometer was calibrated using the standard Au $4f_{7/2}$ peak at 84.0 eV. Survey scans were recorded with a step size of 0.5 eV, and the pass energy was 150 eV. The C 1s peak position (the standard value is 284.6 eV) was used to correct the shifts, if any, in the spectral positions of Zn, O, and N caused due to charging of the samples. Zn, O, and N spectral peaks were deconvoluted using the commercial XPSPEAK41 software with a Shirley-type background. The FTIR study was performed by a USINF JASCO, FT/IR-6100 spectrophotometer.

2.3. Antibacterial Assay. *2.3.1. Microtiter Plate Assay.* The characterized pristine-ZnO and ZnO-H*i* (i = 1, 2, 3, 4) samples were then used to study their biological activity against *E. coli*. The experimental procedures adopted are as follows: the microtiter plate assay was performed to evaluate the effect of pristine-ZnO and ZnO-H*i* (i = 1, 2, 3, 4) on *E. coli*. Bacterial culture was procured from the NCIM, CSIR-NCL, Pune, India. The culture was grown in a nutrient broth (HiMedia, India) at 37 °C under shaking conditions (150 rpm). *E. coli* culture was further maintained as per the supplier's instructions. Before using the bacterial culture, stock solutions of pristine-ZnO and ZnO-H*i* (i = 1, 2, 3, 4) with a 200 μg/mL concentration were prepared in sterile distilled water. These solutions were then ultrasonicated for 1 h for rigorous mixing. Round-bottomed 96-well microtiter polystyrene plates (Tarson, India) were used for further experiments. 100 μL of sterile Muller−Hinton broth (MHB, HiMedia, India) was added to each microtiter plate. 100 μL of L-histidine with a 100 μg/mL concentration was added to the first well of the first row. It was mixed thoroughly, and 100 μL of the mixture was transferred to the second well of the first row to achieve a 50 μg/mL concentration. The mixture in the second well of the first row was thoroughly mixed, and 100 μL of the solution was transferred to the third well of the first row. This process was repeated till the sixth well of the first row. The successive twofold dilution obtained was 100, 50, 25, 12.5, 6.25, and 3.12 μg/mL. After the serial dilution, 50 μL of the overnight-grown *E. coli* culture was used as the inoculum from wells no. 1−6 of the first row. The seventh well of the first row was left as it was with 150 μL of MHB and was considered a negative control. In the eighth well of the first row, 50 μL of optical density (OD) 0.5 McFarland-adjusted *E. coli* culture was added and treated as a positive control. This final volume in each well was maintained at 150 μL. The same exercise was repeated from the second to the sixth row with ZnO and ZnO-H*i* (i = 1, 2, 3, 4) solutions. The experiment was performed in triplicate. These plates were incubated overnight at 37 °C, and an ELISA microtiter plate reader (Spectramax M2, USA) was used to measure the OD at a wavelength of 540 nm. Growth inhibition of *E. coli* at different concentrations was calculated using[30]

$$\text{percentage cell inhibition} = \frac{(A_t - A_b)}{(A_c - A_b)} \times 100\ \% \quad (1)$$

where A_t is the OD of the test compound, A_b is the blank (−ve control), and A_c is the OD of control (+ve control).

2.3.2. Morphological Study of E. coli. Scanning electron microscopy (SEM) was used to study the morphological changes in *E. coli* cells due to their interactions with pristine-ZnO and ZnO-H*i* (i = 1, 2, 3, 4). The protocol used is described in brief as follows: the cells of *E. coli* were grown overnight in MHB, and the OD of 0.5 was adjusted (as per the McFarland standard) and used for the study. From this, 100 μL of the culture was inoculated into five separate tubes having sterile MHB (10 mL) with pristine-ZnO and ZnO-H*i* (i = 1, 2, 3, 4) at a concentration of 100 μg/mL. All these five tubes were considered test samples. The sixth tube containing only fresh sterile MHB (10 mL) inoculated with 100 μL of *E. coli* culture was also considered a control tube. All six tubes were

https://doi.org/10.1021/acsomega.3c01183
ACS Omega 2023, 8, 34354−34363

incubated at 37 °C for 3 h at 150 rpm. After incubation, all six tubes were removed, and the culture broth was centrifuged at 10,000 rpm for 15 min at 4 °C to collect the cell pellets. The pellets were then washed three times with 0.1 M phosphate buffer saline (PBS) (pH 7.4) to remove the traces of MHB. Then, it was fixed in 2.5% (v/v) glutaraldehyde at 4 °C for 4 h and then washed thrice with PBS buffer. Furthermore, dehydration procedures were carried out gradually by treating the cells with ethanol ranging from 10 to 100% (v/v) at 15 min intervals. Samples treated with 100% ethanol were placed on a clean glass slide to examine the morphology of *E. coli* cells (of test and control) under SEM.

2.3.3. ROS Assay. ROS are chemically reactive chemical species having oxygen. ROS are generated as a natural byproduct from the normal metabolism of oxygen. Bacteria are bathed in toxic surroundings having lethal stressors like ROS, H_2O_2, O_2, and OH radicals. Accumulation of ROS leads to lethal activity for many antimicrobial agents. We estimated ROS generated in *E. coli* with the help of previously established protocols described by Ramani et al.[23] In brief, *E. coli* culture was grown in MHB at 37 °C with shaking at 150 rpm, and an OD of 0.5 was adjusted (as per the McFarland standard) and used for the experiment. *E. coli* cells were treated with ZnO and ZnO-H*i* (i = 1, 2, 3, 4) with a 100 μg/mL concentration. Then, liquids of this treated sample were taken out after 90 min of incubation and centrifuged at 6000 rpm for 10 min. The cells were washed twice with PBS and kept in PBS with dichloro-dihydro-fluorescein diacetate—a membrane soluble dye (DCFH-DA)—at 37 °C in the dark condition for 45 min. The specimens were centrifuged at 3000*g* for 5 min and stored in PBS. Intracellular ROS activity was measured for all samples using a flow cytometer (Life Technologies, USA). Intracellular-generated ROS was detected by spotting a change in the fluorescence of DCFH-DA. However, the nonfluorescent material 2′,7′-dichlorofluorescein (H_2DCF) is produced by the reaction of intracellular esterase and DCFH-DA. Intracellular H_2DCF and its oxidation by ROS contribute to fluorescent DCF. It is supervised by a change in fluorescence at 530 nm if the sample is excited by a 488 nm radiation. The observed fluorescence represents a count of ROS in the cell.

3. RESULTS AND DISCUSSION

3.1. XRD Analysis. The XRD pattern of pristine-ZnO and L-histidine-incorporated ZnO samples is shown in Figure 1. Observation of different Bragg reflections indicates that pristine-ZnO and L-histidine incorporated ZnO are polycrystalline. All the diffraction peaks can be indexed to the wurtzite structure of ZnO (JCPDS data card # 36-1451) with the space group $P6_3mc$. No other Bragg diffraction peaks corresponding to either Zn, Zn−OH, $Zn(OH)_2$, or any different phases or complexes were detected, confirming the formation of single-phase pristine-ZnO and L-histidine-incorporated ZnO.

Using the FWHM corresponding to the Bragg reflections of the planes $(10\bar{1}0)$, (0002), and $(10\bar{1}1)$ in pristine-ZnO and L-histidine-modified ZnO, the average particle size (t) is estimated from the modified *Scherrer* formula

$$t = \left(\frac{K\lambda}{\sqrt{\beta_M^2 \beta_S^2} \cos\theta} \right) + \eta \tan \quad (2)$$

where K is the shape factor (0.9), β_M is the measured width of the diffraction line, β_S is the measured width of the diffraction line from the standard sample, and η is the strain in the specimen. The estimated values of average particle size using the modified *Scherrer* formula are shown in Table 1.

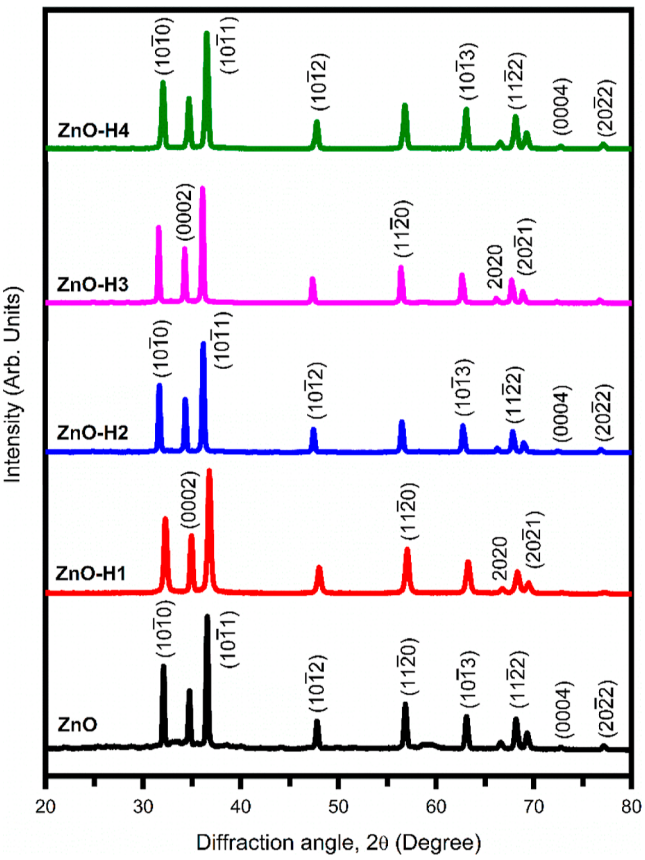

Figure 1. XRD of pristine-ZnO and L-histidine-incorporated ZnO samples.

The XRD patterns of all samples were then subjected to *Rietveld* analysis. Figure 2 shows the *Rietveld* fittings to the XRD patterns. A black line with filled dots indicates the recorded data points, while the solid red line indicates the *Rietveld* fits. The blue line below each XRD pattern suggests the difference in the observed and the *Rietveld* fitted curves, which means good *Rietveld* fitting. Above the blue line are green markers, which show the expected Bragg diffracted peak positions corresponding to different crystallographic orientations of wurtzite ZnO.

Table 1 shows the lattice parameters a and c and the volume of a unit cell of pristine-ZnO and ZnO-H*i* (i = 1, 2, 3, 4) samples estimated from the *Rietveld* analysis. It is observed that the lattice parameters of L-histidine-incorporated ZnO samples increase compared to the pristine-ZnO. The volume of the unit cell also increases substantially. It is an indication of the successful incorporation of L-histidine into ZnO. It is interesting to note that the c/a ratio in all the cases is nearly equal to 1.60, which matches the wurtzite ZnO structure. Due to increased lattice parameters, the unit cell and ZnO lattice volume are expected to be strained, as observed by Brif et al.[31]

For further microstructural analysis, the average crystallite size and strain developed in the samples were calculated using the Williamson−Hall (W−H) method.[32] The observed FWHM broadening of the peaks is the influence of the instrument and sample-dependent factors. To disintegrate the

https://doi.org/10.1021/acsomega.3c01183
ACS Omega 2023, 8, 34354−34363

Table 1. Lattice Parameters (a and c) and Their Ratio (c/a) and Volume of the Unit Cell (V) of Pristine-ZnO and L-Histidine-Incorporated ZnO Samples

Sample	a (Å)	c (Å)	(c/a) ratio	V (Å^3)	t (nm)		strain
					Scherrer formula	W–H plot	
ZnO-pristine	3.26	5.25	1.610	48.39	84	89	1.0×10^{-3}
ZnO-H1	3.30	5.31	1.609	50.07	80	80	1.3×10^{-3}
ZnO-H2	3.35	5.34	1.594	51.90	53	51	1.5×10^{-3}
ZnO-H3	3.35	5.36	1.600	52.10	45	48	1.9×10^{-3}
ZnO-H4	3.36	5.38	1.601	52.60	39	43	2.3×10^{-3}

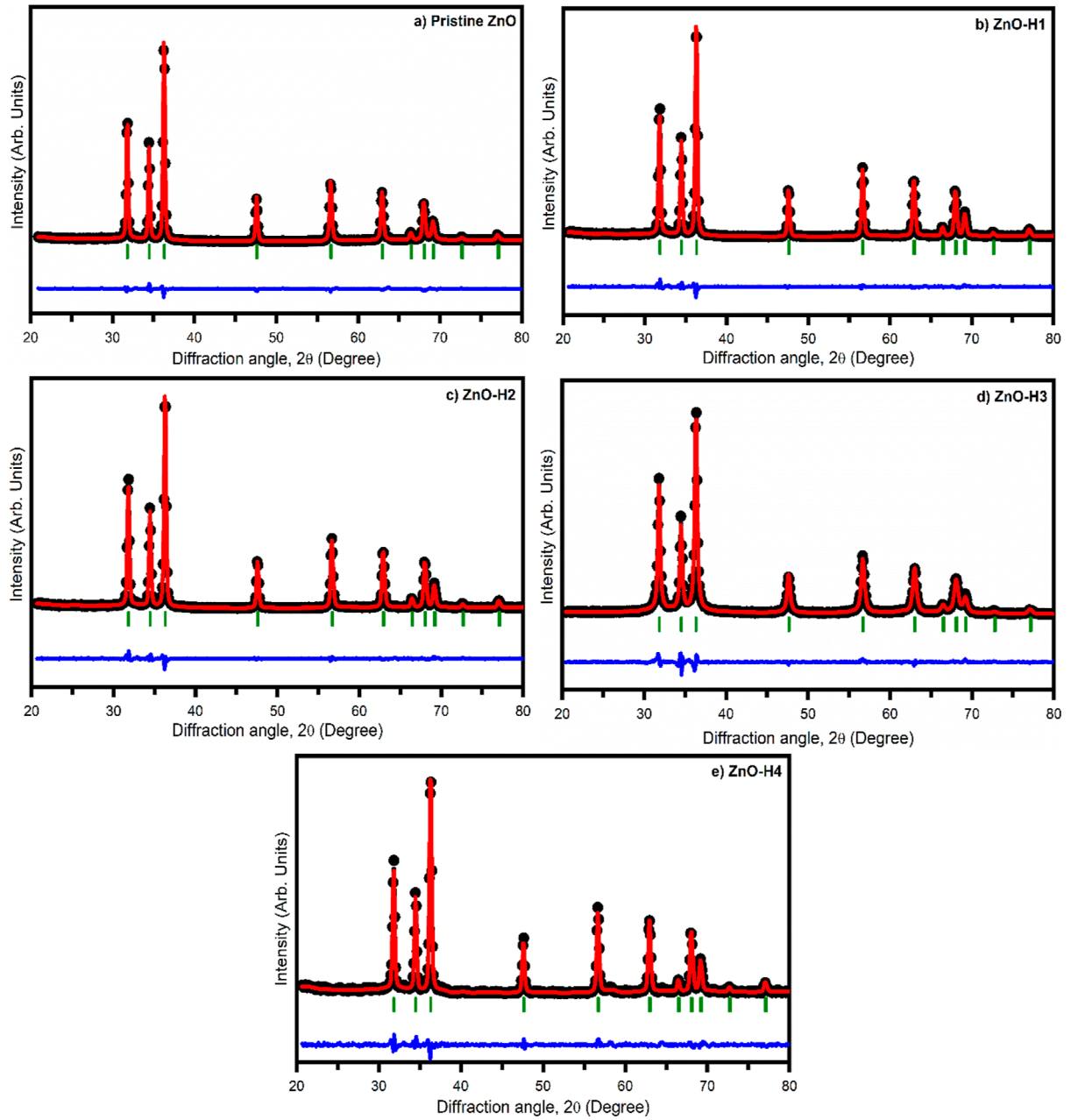

Figure 2. Rietveld-fitted X-ray pattern of pristine-ZnO and L-histidine-incorporated ZnO samples.

effect of instrumental broadening, the observed FWHM is corrected using

$$\beta = [(\beta^2)_{\text{Measured}} - (\beta^2)_{\text{Instrumental}}]^{1/2} \quad (3)$$

where $\beta_{\text{Instrumental}}$ is the broadening contribution due to the instrument. The strain induced in the host has been analyzed by the uniform deformation model of the Williamson–Hall method, wherein $\beta \cos \theta$ is plotted versus 4 sin θ (Figure 3).

The crystalline size and strain are extracted from the intercept and slope of the linear fit, respectively, according to the equation

https://doi.org/10.1021/acsomega.3c01183
ACS Omega 2023, 8, 34354–34363

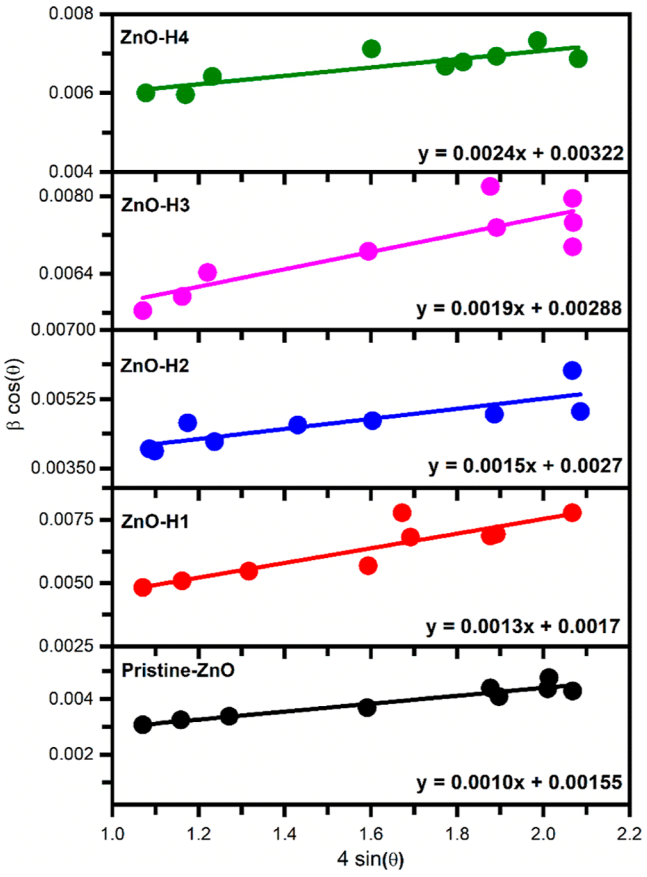

Figure 3. Variation of β cos θ as a function of 4 sin θ of pristine-ZnO and L-histidine-incorporated ZnO samples.

$$\beta\cos\theta = \frac{k\lambda}{D} + 4\epsilon\sin\theta \quad (4)$$

It is noted that the microstrain increases with an increase in L-histidine concentration, whereas the average crystallite size decreases. To release the excess strain, the crystallites break into smaller fragments, thus reducing the average crystallite size. Table 1 shows the decrease in the average crystallite size of ZnO with an increase in the concentration of L-histidine in ZnO. The strain generated in ZnO due to the presence of intracrystalline molecules originated from amino acids. The L-histidine around the crystallites prevents the host's tendency to form larger crystals or prevents the agglomeration among the particles.[30]

3.2. Fourier Transform Infrared (FTIR) Spectroscopy. FTIR spectra of L-histidine, pristine-ZnO, and ZnO-H*i* (*i* = 1, 2, 3, 4) samples were recorded in the 400−4000 cm^{-1} range and are shown in Figure 4.

The FTIR spectra show that the band observed from 430 to 560 cm^{-1} is assigned to the O−Zn−O stretching mode in ZnO.[33] The out-of-plane bending of the −CH bond and antisymmetric stretching of CO_2^{2-} are observed at ∼875 and ∼1572 cm^{-1}, respectively. The vibration of the Zn−O bond is indicated by peaks that appeared at ∼1388 and 1514 cm^{-1}.[34] It confirms the integration of L-histidine with ZnO. The CH_3 rocking mode is observed at ∼1014 cm^{-1}.[33] At ∼1760 cm^{-1}, the C═O vibrational mode is observed.[35] Finally, the C═O═C vibrational mode is observed at ∼2384 cm^{-1}.[36] The absorption band at ∼3300−3500 cm^{-1} is assigned to the −OH group and water on the surface of ZnO nanoparticles.[33] The

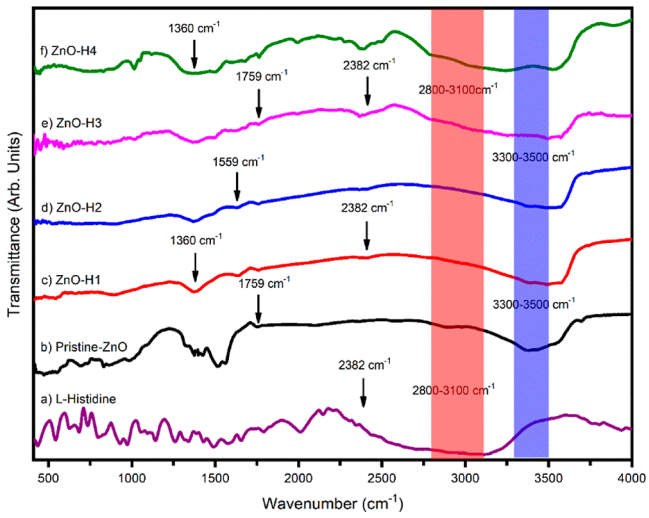

Figure 4. FTIR spectra of (a) L-histidine, (b) pristine-ZnO, (c) ZnO-H1, (d) ZnO-H2, (e) ZnO-H3, and (f) ZnO-H4.

prominent peaks in FTIR spectra are numbered, and their spectral assignment is listed in Table 2.

Table 2. FTIR Transmission Peak Identification

Peak	Wavenumber (cm^{-1})	Assignment
1	430−560	O−Zn−O
2	875	Out-of-plane bending of −CH
3	1014	CH_3 rocking
4	1388	Zn−N vibration bond
5	1514	
6	1572	Antisymmetric stretching of CO_2^{2-}
7	1760	C═O group
8	2384	C═O═C
9	3300−3500	−OH group or water molecule

3.3. FESEM Analysis. The surface morphologies of pristine-ZnO and L-histidine-incorporated ZnO samples were investigated using FESEM. Before imaging, films were coated with Pt by the sputtering method. Figure 5 shows FESEM images of pristine-ZnO and L-histidine-incorporated ZnO samples. The FESEM images for all samples are homogeneous, dense, and free from flaws, cracks, and protrusions. However, the surface morphology changes significantly with an increase in the concentration of L-histidine. The following observations are made from the FESEM analysis; (i) for the pristine-ZnO sample (Figure 5a), a well-defined hexagonal morphology of the crystallites in the form of disks or solid rods is observed. In addition, these crystallites are interlinked, forming more oversized agglomerates. (ii) For L-histidine-incorporated ZnO samples (Figure 5b−e), the typical hexagonal features of the crystallites are no longer visible. The size of the layered structures was found to reduce with the increase in histidine concentration during synthesis. In addition, these crystallites are interlinked, forming more oversized agglomerates.

3.4. XPS Analysis. The electronic structure and chemical properties of pristine-ZnO and L-Histidine-incorporated ZnO samples have been analyzed using high-resolution XPS. XPS spectra were calibrated with the C 1s peak (284.6 eV) as a reference. The typical XPS spectrum of ZnO-H4 is shown in Figure 6.

https://doi.org/10.1021/acsomega.3c01183
ACS Omega 2023, 8, 34354−34363

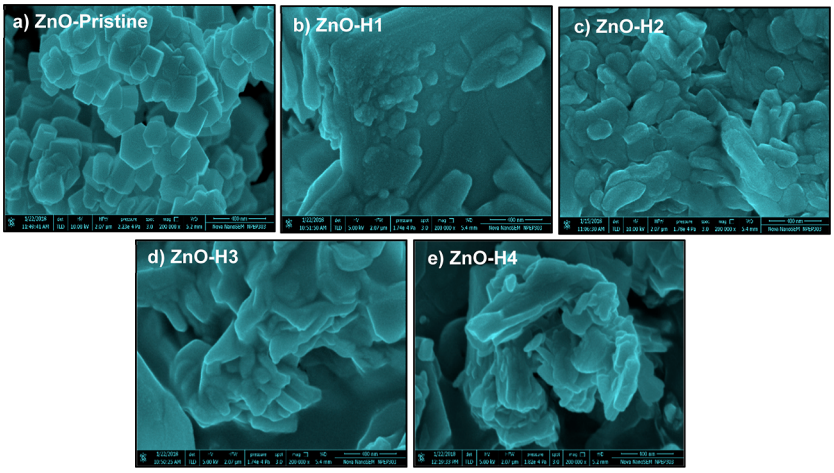

Figure 5. FESEM images of (a) pristine-ZnO, (b) ZnO-H1, (c) ZnO-H2, (d) ZnO-H3, and (e) ZnO-H4.

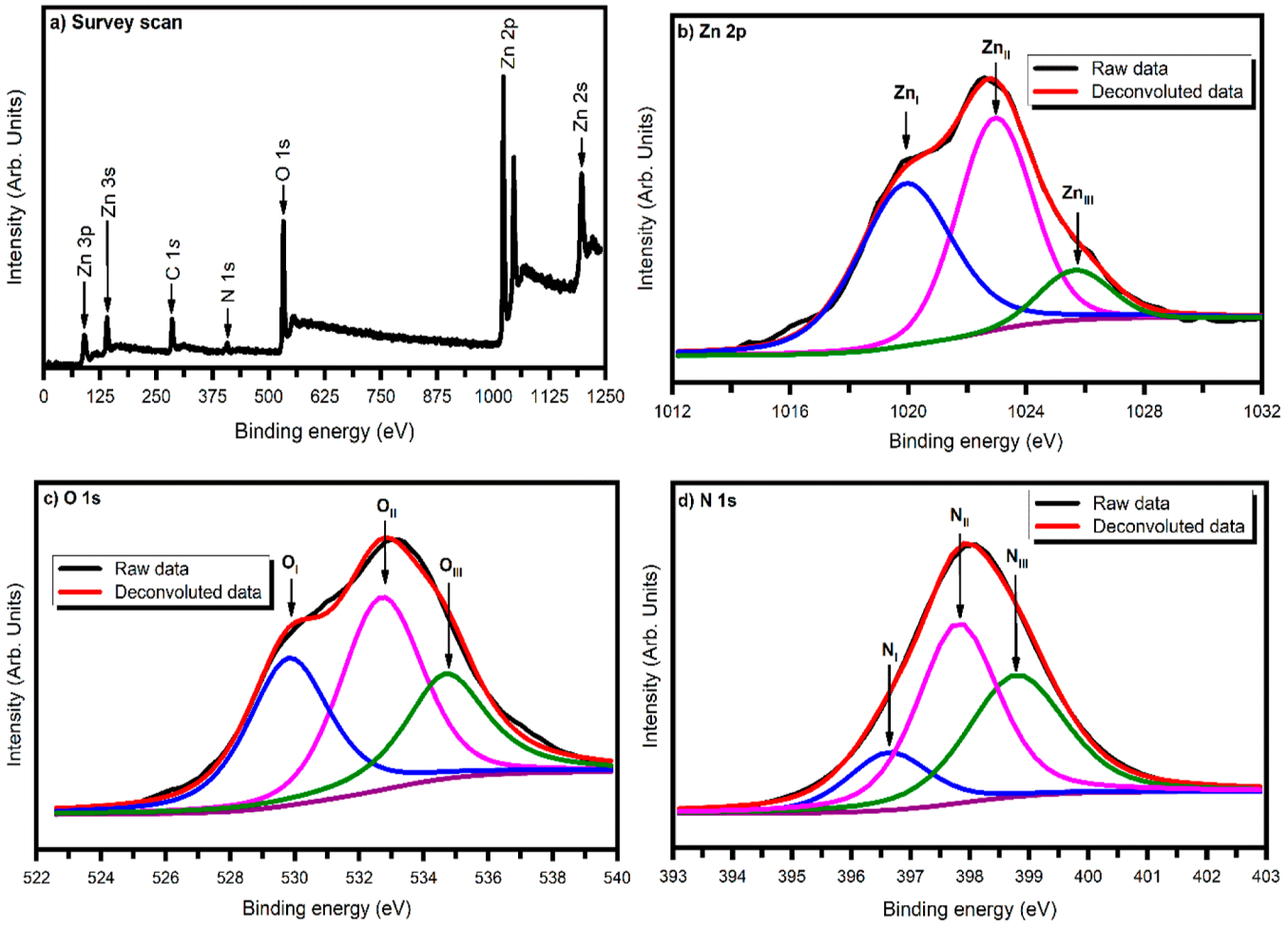

Figure 6. XPS spectra of the ZnO-H4 (a) survey scan in the range 0−1250 eV, (b) narrow scan of Zn 2p3/2 in the range of 10,212−2032 eV, (c) narrow scan of O 1s in the range of 522−540 eV, and (d) narrow scan of N 1s in the range of 393−403 eV.

XPS survey scan of ZnO-H4 recorded in the range of 0−1250 eV is shown in Figure 6a. As seen, the peaks corresponding to Zn (2s, 2p, 3s, 3p, and 3d), C 1s, N 1s, and O 1s orbitals appear in the XPS spectra.[37] No other peaks were observed, signifying the chemical purity of ZnO-H4. Moreover, the spin−orbit-coupled energy states, which correspond to Zn $2p_{3/2}$ and Zn $2p_{1/2}$, were observed at ∼1020.98 and ∼1044.31 eV, respectively, with a characteristic difference of 23.33 eV.[37] It reveals that Zn is present in the Zn^{2+} state in ZnO.[37] Figure 6b shows the deconvoluted Zn 2p spectra. The Zn 2p3/2 spectra could be deconvoluted into three Gaussian−Lorentzian curves depicted as Zn(I), Zn(II), and Zn(III), positioned at ∼1019.5, ∼1022.5, and ∼1025.0 eV, respectively. These peaks can be attributed to Zn in layered basic Zn nitrate, Zn^{2+} in ZnO, and Zn bonded as Zn−O−C═O.[27,37−40] Figure 6c shows the deconvoluted O 1s spectra of

https://doi.org/10.1021/acsomega.3c01183
ACS Omega 2023, 8, 34354−34363

the ZnO-H4 sample. The spectra can be deconvoluted into three Gaussian−Lorentzian curves with their peaks; O(I), O(II), and O(III) are positioned at ∼530.0, ∼532.5, and ∼534.5 eV, respectively. The observed values of binding energy are attributed to O^{2-} (lattice oxygen present in perfect symmetry), O^{2-} (lattice oxygen in distorted symmetry), and the loosely bound oxygen such as adsorbed CO, adsorbed O_2, or adsorbed H_2O on the ZnO surface, respectively.[25,27,35] Thus, oxygen exists in three different chemical environments with varying contributions to the ZnO sample. However, Stevens et al.[41] have shown that the COO− group in L-histidine indicates only a single O 1s peak at ∼531.3 eV, which appears to have been overlaid by the O_2-peaks at ∼530.0 and 532.5 eV. The observation of the N 1s signal in the survey scan shows the presence of L-histidine in ZnO. Figure 6d shows that the deconvoluted N1s spectra of the ZnO-H4 sample can be deconvoluted into three Gaussian−Lorentzian curves at ∼396, ∼397, and ∼399 eV. These peaks correspond to the N−Zn, N−C (N=C−NH of histidine), and N−H (C−NH^+ of L-histidine) bonds, respectively.[10,42] Furthermore, a similar N 1s peak has been observed in all ZnO-H*i* (*i* = 1, 2, 3, 4) samples. These observations of core-level spectra of Zn, O, and N atoms reveal the incisively complex bonding of the constituent atoms in the synthesized samples.

3.5. Microtiter Plate Assay. Various mechanisms have been reported in the literature regarding the antibacterial activity of nanomaterials.[43] It includes the direct physical interaction of extremely sharp edges of nanomaterials with a cell wall membrane,[44] ROS generation,[45,46] trapping the bacteria within the aggregated nanomaterials,[47] oxidative stress,[48] interruptions in the glycolysis process of the bacteria,[49] DNA damaging,[50] Zn ion release,[51] contributions in generation/explosion of nanobubbles,[52] and so forth. Single or multiple modes of mechanism may occur during the antibacterial activity of nanomaterials. Figure 7 shows the

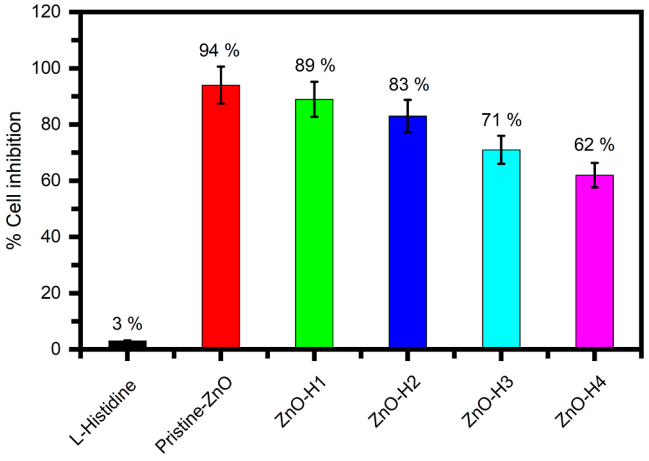

Figure 7. Variation in inhibition of *E. coli* cells treated with ZnO and L-histidine-incorporated ZnO samples.

variation in percentage growth inhibition of *E. coli* after treatment with 100 μg/mL ZnO and L-histidine-incorporated ZnO. The reproducibility of growth inhibition of *E. coli* was confirmed by repeating the experiment under the same set of parameters three times. The growth inhibition values were the same within the experimental error (±5%). The error bars in the figure are derived from the differences obtained in growth inhibition of *E. coli* by repeating the treatment under the same set of parameters with $p \leq 0.05$. It is evident from the bar graph that the ZnO solution shows the highest percentage of inhibition (94%). Furthermore, the figure shows that the antibacterial activity decreases consistently with an increased concentration of histidine incorporated with ZnO. In other words, the toxicity of ZnO is reduced from 94 to 89% for ZnO-H1, 83% for ZnO-H2, 71% for ZnO-H3, and 62% for ZnO-H4. The decrease in the antibacterial activity may be due to the wrapping of the L-histidine molecule around the ZnO nanoparticles after binding to it.

The intermediate layer of L-histidine reduces the interaction of the ZnO particles with *E. coli*; hence, the toxicity of ZnO is altered significantly by successfully integrating L-histidine with ZnO nanocrystals, thus protecting *E. coli*. Dadi et al.[53] also reported similar results of the strong antibacterial activity of ZnO and CuO nanoparticles. We believe that the dominant mechanism in the present work for the antibacterial activity of L-histidine incorporated with ZnO is the ROS (discussed later).

3.6. Morphological Study of *E. coli*. Figure 8 shows the scanning electron micrographs of *E. coli*, *E. coli* cells treated with a 100 μg/mL solution of ZnO, and *E. coli* cells treated with a 100 μg/mL solution of ZnO-H*i* (*i* = 1, 2, 3, 4), respectively. Figure 8a shows the rod-shaped morphology of *E. coli*. However, the same intact morphology is no longer seen in Figure 8b, which is treated with a 100 μg/mL solution of ZnO. It appears that the *E. coli* cells are ruptured because of ZnO. A similar observation can be made from Figure 8c. However, as the concentration of L-histidine incorporated with ZnO-H*i* increases (Figure 8d−f), the *E. coli* cells are not completely destroyed as it is observed in ZnO and ZnO-H1 (Figure 8b,c). These results suggest the antibacterial activity or toxicity reduction of the L-histidine-incorporated ZnO samples.

3.7. ROS Assay. The generation of ROS is one of the unique mechanisms displayed by several antimicrobial agents contributing toward their toxicity in bacteria.[50] Additionally, the generation of the superoxide anion (O^{2-}), hydrogen peroxide (H_2O_2), and hydroxide (OH^-) also contributes to the toxicity of antimicrobial agents. Sirelkhatim et al.[54] have given a detailed explanation of the complete phenomenon. Fluorescent marker-labeled cells or particle absorbs the light, and the side scattered light intensity in flow cytometry displays the cell's intracellular density. The graph of mean fluorescence intensity for ZnO and other samples is shown in Figure 9.

It was observed that there was a sharp change in the fluorescence of the DCFH-DA dye when the *E. coli* cells were treated with ZnO and ZnO-H*i* (*i* = 1, 2, 3, 4) with a concentration of 100 μg/mL. Furthermore, the ROS generated in *E. coli* cells was found to reduce with increased concentration of L-histidine in ZnO nanoparticles. The cellular interaction with these compounds is lower than in pristine-ZnO, indicating the ubiquitous mechanism of cell death through ROS-mediated membrane damage.[23] Furthermore, the antibacterial activity reduces as the concentration of L-histidine incorporated with ZnO increases. The results obtained from ROS studies further support the observation of the microtiter plate assay and SEM results. These studies strongly suggest that combining L-histidine in ZnO reduces the toxicity of ZnO to *E. coli*.

The results show a successful synthesis of pristine-ZnO and L-histidine-incorporated ZnO using an open aqueous solution bath technique at 95 °C for antibacterial activity with a Gram-negative model organism, *E. coli*. Further studies can be

https://doi.org/10.1021/acsomega.3c01183
ACS Omega 2023, 8, 34354−34363

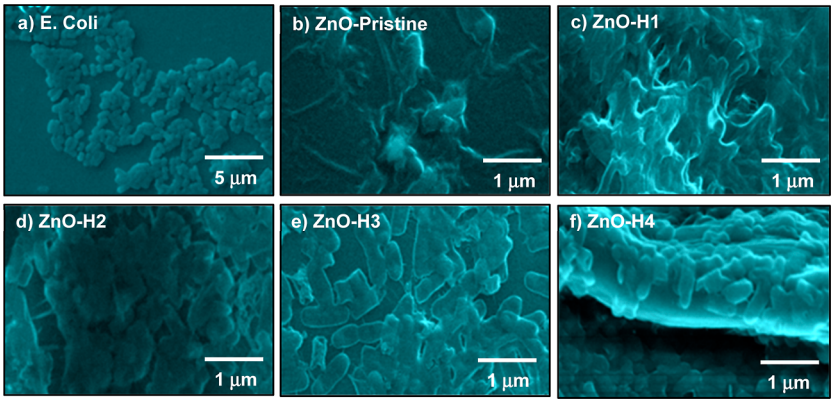

Figure 8. Scanning electron micrographs presenting the (a) *E. coli* cells, (b) effect of ZnO on *E. coli*, and (c–f) effect of ZnO-H*i* (*i* = 1, 2, 3, 4) on *E. coli*.

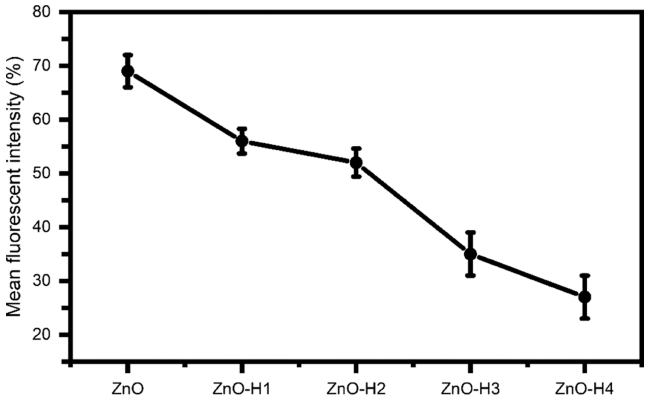

Figure 9. Intracellular ROS for pristine-ZnO and L-histidine-incorporated ZnO samples.

extended on antibacterial activity with a Gram-positive model organism, *E. coli*. During the experimentation, we observed the nonuniform size distribution of ZnO nanoparticles. Therefore, we think that different process parameters of an open aqueous solution bath technique need to be studied to produce a uniform size of the nanoparticles by varying the ratio of metal salts, pH, and temperature during the synthesis process. The investigation also can be carried out in the presence of a natural stabilizing agent to produce better dispersion of ZnO nanoparticles. Further studies on the antibacterial activity on the efficiency of ZnO against pathogenic bacterium and fungi, including the changes in ZnO morphology, can be possible for understanding the inactivation effect of ZnO nanoparticles against pathogenic microorganisms.

4. CONCLUSIONS

Pristine-ZnO and L-histidine-incorporated ZnO were synthesized using an aqueous solution bath method. XRD analysis revealed the formation of polycrystalline wurtzite ZnO. The increased L-histidine concentration showed changes in the structural properties of ZnO-incorporated L-histidine samples. FTIR analysis showed the vibration signals of Zn–O, Zn–N, carboxyl groups, and –OH groups. Upon incorporation of L-histidine with ZnO, it showed a significant change in the surface morphology. The XPS analysis revealed the bonding of Zn, O, and N in three different environments. Finally, the microbial activity of these samples was investigated using *E. coli* as a Gram-negative model organism which showed up to 94% growth inhibition. However, L-histidine incorporated in ZnO showed reduced antibacterial activity. The flow cytometry studies during the interaction of ZnO and *E. coli* confirmed the generation of ROS, validating its antibacterial activity. However, the generation of ROS declined with an increase in L-histidine concentration, signifying a reduction in the toxicity of ZnO. The results show the potential application of the synthesized material in tissue engineering, medical implantation, and drug delivery.

■ ASSOCIATED CONTENT

Supporting Information

The Supporting Information is available free of charge at https://pubs.acs.org/doi/10.1021/acsomega.3c01183.

Materials and synthesis and particle size distribution (PDF)

■ AUTHOR INFORMATION

Corresponding Authors

Shashikant P. Patole – *Department of Physics, Khalifa University of Science and Technology, Abu Dhabi 127788, UAE*; orcid.org/0000-0001-6669-6635; Email: shashikant.patole@ku.ac.ae

Sandesh R. Jadkar – *Department of Physics, Savitribai Phule Pune University, Pune 411 007, India*; Email: sandesh@physics.unipune.ac.in

Authors

Shraddha Mahakal – *Department of Physics, Savitribai Phule Pune University, Pune 411 007, India*

Habib M. Pathan – *Department of Physics, Savitribai Phule Pune University, Pune 411 007, India*

Mohit Prasad – *Department of Physics, Savitribai Phule Pune University, Pune 411 007, India; Department of Applied Science and Humanities, Pimpri Chinchwad College Of Engineering (PCCOE), Pune 411 004, India*

Sachin Rondiya – *Department of Materials Engineering, Indian Institute of Science, Bangalore 560 012, India*

Complete contact information is available at: https://pubs.acs.org/10.1021/acsomega.3c01183

Author Contributions

Shraddha Mahakal: methodology, formal analysis, investigation, data curation, writing-original draft. Habib Pathan: validation, formal analysis, investigation. Mohit Prasad: formal

https://doi.org/10.1021/acsomega.3c01183
ACS Omega 2023, 8, 34354–34363

analysis, investigation, and editing. Sachin Rondiya: formal analysis, investigation. Shashikant Patole: writing-review and editing. Sandesh Jadkar: visualization, writing-review, editing, supervision, funding acquisition.

Notes

The authors declare no competing financial interest.

■ ACKNOWLEDGMENTS

S.M. acknowledges the University Grants Commission (UGC), Government of India, New Delhi, India, and A. A. College, Manchar, Maharashtra, India, for the opportunity to carry out the present research work under the faculty improvement program (FIP). In addition, the authors acknowledge Raja Ramanna Center for Advanced Technology (RRCAT), Indore, India, for helping in recording the XPS spectra. Finally, M.P. and S.J. thank the Indo-French Centre for the Promotion of Advanced Research-CEFIPRA, Department of Science and Technology, New Delhi, for special financial support. S.P.P. would like to thank Khalifa University for its financial support through the internal fund for high-quality publications.

■ REFERENCES

(1) Speaks, D. T. Effect of concentration, aging, and annealing on sol-gel ZnO and Al-doped ZnO thin films. *Int. J. Mech. Mater. Eng.* **2020**, *15*, 2.
(2) Schneider, J. J.; Hoffmann, R. C.; Engstler, J.; Soffke, O.; Jaegermann, W.; Issanin, A.; Klyszcz, A. A printed and flexible field-effect transistor device with nanoscale zinc oxide as active semiconductor material. *Adv. Mater.* **2008**, *20*, 3383−3387.
(3) Rajab, F. H.; Taha, R. M.; Khashan, K. S.; Hadi, A. A.; Mahdi, R. O. Laser induced hydrothermal growth of ZnO rods for UV detector application. *Opt. Quant. Electron.* **2023**, *55*, 208.
(4) Sirelkhatim, A.; Mahmud, S.; Seeni, A.; Kaus, N. H. M.; Ann, L. C.; Bakhori, S. K. M.; Hasan, H.; Mohamad, D. Review on zinc oxide nanoparticles: antibacterial activity and toxicity mechanism. *Nano-Micro Lett.* **2015**, *7*, 219−242.
(5) Tereshchenko, A.; Bechelany, M.; Viter, R.; Khranovskyy, V.; Smyntyna, V.; Starodub, N.; Yakimova, R. Optical biosensors based on ZnO nanostructures: advantages and perspectives. A review. *Sens. Actuators, B* **2016**, *229*, 664−677.
(6) Huang, X.; Zheng, X.; Xu, Z.; Yi, C. ZnO-based nanocarriers for drug delivery application: From passive to smart strategies. *Int. J. Pharm.* **2017**, *534*, 190−194.
(7) Uthirakumar, P.; Kim, H. G.; Hong, C. H. Zinc oxide nanostructures derived from a simple solution method for solar cells and LEDs. *Chem. Eng. J.* **2009**, *155*, 910−915.
(8) Fan, Z.; Lu, J. G. Zinc Oxide Nanostructures: Synthesis and Properties. *J. Nanosci. Nanotechnol.* **2005**, *5*, 1561−1573.
(9) Vega, N. C.; Straube, B.; Marin-Ramirez, O.; Comedi, D. Low temperature chemical vapor deposition as a sustainable method to obtain c-oriented and highly UV luminescent ZnO thin films. *Mater. Lett.* **2023**, *333*, 133684.
(10) Dong, Y.; Zhou, M.; Zhou, H.; Deng, Y.; Wang, X.; Zhang, X. Facile synthesis of metal organic decomposition Al-doped ZnO ink for inkjet printing and fabrication of highly transparent conductive film. *Ceram. Int.* **2023**, *49*, 12687−12695.
(11) Mejri, I. H.; Omri, K.; Ghiloufi, I.; Silva, J. P. B.; Gomes, M. J. M.; Mir, L. E. Resistive switching behavior in ZnO:Ca thin films deposited by a pulsed laser deposition technique. *Appl. Phys. A* **2023**, *129*, 210.
(12) Ayon, S. A.; Billah, M. M.; Hossain, M. N. Effect of annealing temperature on structural, optical, and photocatalytic properties of modified sol−gel-driven ZnO nanoparticles. *Surf. Interface Anal.* **2023**, *55*, 1−7.
(13) Hu, Y.; Sun, L.; Liu, Z.; Liu, T. Controlled solvothermal synthesis of ZnO nanoparticles using non-destructive Mg-based channel templates for enhanced photocatalytic performance. *Mater. Chem. Phys.* **2023**, *299*, 127525.
(14) Lad, P.; Pathak, V.; Thakkar, A. B.; Thakor, P.; Deshpande, M. P.; Pandya, S. ZnO Nanoparticles Synthesized by Precipitation Method for Solar-Driven Photodegradation of Methylene Blue Dye and Its Potential as an Anticancer Agent. *Braz. J. Phys.* **2023**, *53*, 63.
(15) Hajiashrafi, S.; Motakef Kazemi, N. Preparation and evaluation of ZnO nanoparticles by thermal decomposition of MOF-5. *Heliyon* **2019**, *5*, No. e02152.
(16) Kołodziejczak-Radzimska, A.; Jesionowski, T. Zinc oxide-from synthesis to application: A Review. *Materials* **2014**, *7*, 2833−2881.
(17) Ehsan, S.; Sajjad, M. Bioinspired synthesis of zinc oxide nanoparticle and its combined efficacy with different antibiotics against multidrug-resistant bacteria. *J. Biomater. Nanobiotechnology* **2017**, *08*, 159−175.
(18) Velmurugan, P.; Park, J.-H.; Lee, S.-M.; Jang, J.-S.; Yi, Y.-J.; Han, S.-S.; Lee, S.-H.; Cho, K.-M.; Cho, M.; Oh, B.-T. Phytofabrication of bioinspired zinc oxide nanocrystals for biomedical application. *Artif. Cells, Nanomed. Biotechnol.* **2016**, *44*, 1529−1536.
(19) Maruyama, T.; Fujimoto, Y.; Maekawa, T. Synthesis of gold nanoparticles using various amino acids. *J. Colloid Interface Sci.* **2015**, *447*, 254−257.
(20) Klekotka, U.; Satuła, D.; Basa, A.; Kalska-Szostko, B. Importance of surfactant quantity and quality on growth regime of iron oxide nanoparticles. *Materials* **2020**, *13*, 1747.
(21) Nguyen, M. A.; Hughes, Z. E.; Liu, Y.; Li, Y.; Swihart, M. T.; Knecht, M. R.; Walsh, T. R. Peptide-mediated growth and dispersion of Au nanoparticles in water via sequence engineering. *J. Phys. Chem. C* **2018**, *122*, 11532−11542.
(22) Guo, Y.; Lin, S.; Li, X.; Liu, Y. Amino acids assisted hydrothermal synthesis of hierarchically structured ZnO with enhanced photocatalytic activities. *Appl. Surf. Sci.* **2016**, *384*, 83−91.
(23) Ramani, M.; Ponnusamy, S.; Muthamizhchelvan, C.; Marsili, E. Amino acid-mediated synthesis of zinc oxide nanostructures and evaluation of their facet-dependent antimicrobial activity. *Colloids and Surfaces B: Biointerfaces* **2014**, *117*, 233−239.
(24) Gerstel, P.; Hoffmann, R. C.; Lipowsky, P.; Jeurgens, L. P.; Bill, J.; Aldinger, F. Mineralization from aqueous solutions of zinc salts directed by amino acids and peptides. *Chem. Mater.* **2006**, *18*, 179−186.
(25) Brif, A.; Ankonina, G.; Drathen, C.; Pokroy, B. Bio-inspired band gap engineering of zinc oxide by intracrystalline incorporation of amino acids. *Adv. Mater.* **2014**, *26*, 477−481.
(26) Umetsu, M.; Mizuta, M.; Tsumoto, K.; Ohara, S.; Takami, S.; Watanabe, H.; Kumagai, I.; Adschiri, T. Bioassisted room-temperature immobilization and mineralization of zinc oxide-The structural ordering of ZnO nanoparticles into a flower-type morphology. *Adv. Mater.* **2005**, *17*, 2571−2575.
(27) Limo, M. J.; Sola-Rabada, A.; Boix, E.; Thota, V.; Westcott, Z. C.; Puddu, V.; Perry, C. C. Interactions between metal oxides and biomolecules: From fundamental understanding to applications. *Chem. Rev.* **2018**, *118*, 11118−11193.
(28) Verma, S. K.; Jha, E.; Panda, P. K.; Das, J. K.; Thirumurugan, A.; Suar, M.; Parashar, S. K. S. Molecular aspects of core-shell intrinsic defect induced enhanced antibacterial activity of ZnO nanocrystals. *Nanomed. J.* **2018**, *13*, 43−68.
(29) Babitha, N.; Priya, L. S.; Christy, S. R.; Manikandan, A.; Dinesh, A.; Durka, M.; Arunadevi, S. Enhanced antibacterial activity and photocatalytic properties of ZnO Nanoparticles: Pedalium murex plant extract-assisted synthesis. *J. Nanosci. Nanotechnol.* **2019**, *19*, 2888−2894.
(30) Patel, S.; Gheewala, N.; Suthar, A.; Shah, A. In-vitro cytotoxicity activity of solanum nigrum extract against hela cell line and vero cell line. *Int. J. Pharm. Pharmaceut. Sci.* **2009**, *1*, 38−46.
(31) Brif, A.; Bloch, L.; Pokroy, B. Bio-inspired engineering of a zinc oxide/amino acid composite: synchrotron microstructure study. *CrystEngComm* **2014**, *16*, 3268−3273.

https://doi.org/10.1021/acsomega.3c01183
ACS Omega 2023, 8, 34354−34363

(32) Kibasomba, P. M.; Dhlamini, S.; Maaza, M.; Liu, C. P.; Rashad, M. M.; Rayan, D. A.; Mwakikunga, B. W. Strain and grain size of TiO2 nanoparticles from TEM, Raman spectroscopy and XRD: The revisiting of the Williamson-Hall plot method. *Results Phys.* **2018**, *9*, 628−635.
(33) Liang, M.; Limo, M.; Sola-Rabada, A.; Roe, M.; Perry, C. New Insights into the Mechanism of ZnO Formation from Aqueous Solutions of Zinc Acetate and Zinc Nitrate. *Chem. Mater.* **2014**, *26*, 4119−4129.
(34) Lavand, A. B.; Malghe, Y. S. Synthesis, characterization and visible light photocatalytic activity of nitrogen-doped zinc oxide nanospheres. *J. Asian Ceram. Soc.* **2015**, *3*, 305−310.
(35) Zhu, Y.; Apostoluk, A.; Gautier, P.; Valette, A.; Omar, L.; Cornier, T.; Bluet, J. M.; Masenelli-Varlot, K.; Daniele, S.; Masenelli, B. Intense visible emission from ZnO/PAAX (X = H or Na) nanocomposite synthesized via a simple and scalable sol-gel method. *Sci. Rep.* **2016**, *6*, 23557.
(36) Gayathri, S.; Ghosh, O. S. N.; Sathishkumar, S.; Sudhakara, P.; Jayaramudu, J.; Ray, S. S.; Viswanath, A. K. Investigation of physicochemical properties of Ag-doped ZnO nanoparticles prepared by chemical route. *Appl. Sci. Lett.* **2015**, *1*, 8−13.
(37) Moulder, J. F.; Stickle, W. F.; Sobol, P. E.; Bomben, K. D. *Handbook of X-Ray Photoelectron Spectroscopy*; Chastain, J., Ed.; Perkin-Elmer Corporation: Minnesota, 1992.
(38) Baier, J.; Naumburg, T.; Blumenstein, N. J.; Jeurgens, L. P. H.; Welzel, U.; Do, T. A.; Pleiss, J. Bio-inspired mineralization of zinc oxide in the presence of ZnO-binding peptides. *Biointerface Res. Appl. Chem.* **2012**, *2*, 380−391. https://hdl.handle.net/11858/00-001M-0000-000E-BAC7-6
(39) Dupin, J. C.; Gonbeau, D.; Vinatier, P.; Levasseur, A. Systematic XPS studies of metal oxides, hydroxides, and peroxides. *Phys. Chem. Chem. Phys.* **2000**, *2*, 1319−1324.
(40) Liang, M. K.; Limo, M. J.; Sola-Rabada, A.; Roe, M. J.; Perry, C. C. New insights into the mechanism of ZnO formation from aqueous solutions of zinc acetate and zinc nitrate. *Chem. Mater.* **2014**, *26*, 4119−4129.
(41) Stevens, J. S.; de Luca, A. C.; Pelendritis, M.; Terenghi, G.; Downes, S.; Schroeder, S. L. M.; Schroeder, S. L. M. Quantitative analysis of complex amino acids and RGD peptides by X-ray photoelectron spectroscopy (XPS). *Surf. Interface Anal.* **2013**, *45*, 1238−1246.
(42) Bhirud, A. P.; Sathaye, S. D.; Waichal, R. P.; Nikam, L. K.; Kale, B. B. An eco-friendly, highly stable and efficient nanostructured p-type N-doped ZnO photocatalyst for environmentally benign solar hydrogen production. *Green Chem.* **2012**, *14*, 2790−2898.
(43) Oves, M.; Ansari, M. O.; Ansari, M. S.; Memić, A. Graphene@ Curcumin-Copper Paintable Coatings for the Prevention of Nosocomial Microbial Infection. *Molecules* **2023**, *28*, 2814.
(44) Akhavan, O.; Ghaderi, E. Toxicity of graphene and graphene oxide nanowalls against bacteria. *ACS Nano* **2010**, *4*, 5731−5736.
(45) Dutta, T.; Sarkar, R.; Pakhira, B.; Ghosh, S.; Sarkar, R.; Barui, A.; Sarkar, S. ROS generation by reduced graphene oxide (rGO) induced by visible light showing antibacterial activity: Comparison with graphene oxide (GO). *RSC Adv.* **2015**, *5*, 80192−80195.
(46) Lakshmi Prasanna, V.; Vijayaraghavan, R. Insight into the mechanism of antibacterial activity of ZnO: Surface defects mediated reactive oxygen species even in the dark. *Langmuir* **2015**, *31*, 9155−9162.
(47) Mohammed, H.; Kumar, A.; Bekyarova, E.; Al-Hadeethi, Y.; Zhang, X.; Chen, M.; Ansari, M. S.; Cochis, A.; Rimondini, L. Antimicrobial mechanisms and effectiveness of graphene and graphene-functionalized biomaterials. A scope review. *Front. Bioeng. Biotechnol.* **2020**, *8*, 465.
(48) Liu, S.; Zeng, T.H.; Hofmann, M.; Burcombe, E.; Wei, J.; Jiang, R.; Kong, J.; Chen, Y. Antibacterial activity of graphite, graphite oxide, graphene oxide, and reduced graphene oxide: Membrane and oxidative stress. *ACS Nano* **2011**, *5*, 6971−6980.
(49) Akhavan, O.; Ghaderi, E. Escherichia coli bacteria reduce graphene oxide to bactericidal graphene in a self-limiting manner. *Carbon* **2012**, *50*, 1853−1860.
(50) Kumar, A.; Pandey, A.; Singh, S. S.; Shanker, R.; Dhawan, A. Engineered ZnO and TiO_2 nanoparticles induce oxidative stress and DNA damage leading to reduced viability of Escherichia coli. *Free Radic. Biol. Med.* **2011**, *51*, 1872−1881.
(51) Wang, Y.; Cao, A.; Jiang, Y.; Zhang, X.; Liu, J.; Liu, Y.; Wang, H. Superior antibacterial activity of zinc oxide/graphene oxide composites originating from high zinc concentration localized around bacteria. *ACS Appl. Mater. Interfaces* **2014**, *6*, 2791−2798.
(52) Jannesari, M.; Akhavan, O.; Madaah Hosseini, H. R.; Bakhshi, B. Graphene/CuO_2 nanoshuttles with controllable release of oxygen nanobubbles promoting interruption of bacterial respiration. *ACS Appl. Mater. Interfaces* **2020**, *12*, 35813−35825.
(53) Dadi, R.; Azouani, R.; Traore, M.; Mielcarek, C.; Kanaev, A. Antibacterial activity of ZnO and CuO nanoparticles against gram-positive and gram-negative strains. *Mater. Sci. Eng. C* **2019**, *104*, 109968.
(54) Sirelkhatim, A.; Mahmud, S.; Seeni, A.; Kaus, N. H. M.; Ann, L. C.; Bakhori, S. K. M.; Hasan, H.; Mohamad, D. Review on Zinc Oxide Nanoparticles: Antibacterial Activity and Toxicity Mechanism. *Nano-Micro Lett.* **2015**, *7*, 219−242.

https://doi.org/10.1021/acsomega.3c01183
ACS Omega 2023, 8, 34354−34363